An axisymmetric gravitational collapse code

Matthew W Choptuik[1], **Eric W Hirschmann**[2], **Steven L Liebling**[3] **and Frans Pretorius**[4]

[1] CIAR Cosmology and Gravity Program, Department of Physics and Astronomy,
University of British Columbia, Vancouver BC, V6T 1Z1 Canada
[2] Department of Physics and Astronomy, Brigham Young University, Provo, UT 84604, USA
[3] Southampton College, Long Island University, Southampton, NY 11968, USA
[4] Theoretical Astrophysics, California Institute of Technology, Pasadena, CA 91125, USA

Abstract
We present a new numerical code designed to solve the Einstein field equations for axisymmetric spacetimes. The long-term goal of this project is to construct a code that will be capable of studying many problems of interest in axisymmetry, including gravitational collapse, critical phenomena, investigations of cosmic censorship and head-on black-hole collisions. Our objective here is to detail the (2+1)+1 formalism we use to arrive at the corresponding system of equations and the numerical methods we use to solve them. We are able to obtain stable evolution, despite the singular nature of the coordinate system on the axis, by enforcing appropriate regularity conditions on all variables and by adding numerical dissipation to hyperbolic equations.

PACS numbers: 04.25.Dm, 04.40.−b, 04.70.Bw

1. Introduction

In this paper we introduce a numerical code designed to solve the Einstein field equations for axisymmetric spacetimes. Even though the predominant focus in numerical relativity in recent years has been to study situations of relevance to gravitational wave detection, and hence lacking symmetries, there are still numerous interesting problems, both physical and computational, that can be tackled with an axisymmetric code. The advantages of restricting the full 3D problem to axisymmetry (2D) are that the complexity and number of equations are reduced, as are the computational requirements compared to solving a similar problem in 3D.

Prior numerical studies of axisymmetric spacetimes include head-on black-hole collisions [1–6], collapse of rotating fluid stars [7–11], the evolution of collisionless particles applied to study the stability of star clusters [12] and the validity of cosmic censorship [13], evolution of gravitational waves [14, 15], black-hole-matter–gravitational wave interactions [16–19], and the formation of black holes through gravitational wave collapse [20] and corresponding critical behaviour at the threshold of formation [21].

Our goals for creating a new axisymmetric code are not only to explore a wider range of phenomena than those studied before, but also to provide a framework to add adaptive mesh refinement (AMR) and black-hole excision to allow more thorough and detailed investigations than prior works.

The outline of the rest of the paper is as follows. In section 2 we describe the (2+1)+1 decomposition [22, 23] of spacetime that we adopt to arrive at our system of equations. The (2+1)+1 formalism is the familiar ADM space+time decomposition (in this case 2+1) applied to a dimensionally reduced spacetime obtained by dividing out the axial Killing vector, following a method devised by Geroch [24]. In section 3 we specialize the equations to our chosen coordinate system, namely cylindrical coordinates with a conformally flat 2-metric. At this stage we do not model spacetimes with angular momentum, and we include a massless scalar field for the matter source. In section 4 we discuss how we search for apparent horizons during evolution. In section 5 we describe our numerical implementation of the set of equations derived in section 3. A variety of tests of our code are presented in section 6, which is followed by conclusions in section 7. Some details concerning our finite difference approximations, solution of elliptic equations via the multi-grid technique and a spherically symmetric code used for testing purposes are given in appendices A and B. Unless otherwise specfied, we use the conventions adopted by Misner *et al* [25], and use geometric units, where $G = c = 1$.

2. The (2+1)+1 formalism

The most common approach in numerical relativity is to perform the so-called 3+1, or ADM, split of the spacetime that one would like to evolve. In this procedure, a timelike vector field is chosen together with spatial hypersurfaces that foliate the spacetime. If axisymmetry is assumed, it is usually incorporated once the ADM decomposition has been done, and is reflected in the independence of the various metric and matter quantities on the ignorable, angular coordinate, φ.

Our approach, which follows Geroch [24] and Nakamura *et al* [9], reverses this procedure. We assume axisymmetry from the outset and perform a reduction of the spacetime based on this assumption. Once we have projected out the symmetry, we perform an ADM-like split (now a 2+1 split) of the remaining 3-manifold.

More specifically, we begin with a four-dimensional spacetime metric[5] $\gamma_{\mu\nu}$ on our manifold $\mathcal{M}$. The axisymmetry is realized in the existence of a spacelike Killing vector

$$X^\mu = \left(\frac{\partial}{\partial\varphi}\right)^\mu,$$

(1)

with closed orbits. We define the projection operator $g_{\mu\nu}$, allowing us to project tensors from the four-dimensional manifold $\mathcal{M}$ with metric $\gamma_{\mu\nu}$ to a three-dimensional manifold $\mathcal{M}/S^1$ with metric g_{ab}, as

$$g_{\mu\nu} = \gamma_{\mu\nu} - \frac{1}{s^2}X_\mu X_\nu,$$

(2)

where s is the norm of the Killing vector

$$s^2 = X^\mu X_\mu.$$

(3)

With the definition of the vector

$$Y_\mu = \frac{1}{s^2}X_\mu,$$

(4)

[5] Note that we will use Greek letters to denote coordinates in the full 4-manifold and Latin letters to denote coordinates in the reduced 3-manifold.

the metric on the full, four-dimensional spacetime can be written as

$$\gamma_{\mu\nu} = \begin{pmatrix} g_{ab} + s^2 Y_a Y_b & s^2 Y_a \\ s^2 Y_b & s^2 \end{pmatrix}. \tag{5}$$

Projecting, or dividing out the symmetry amounts to expressing four-dimensional quantities in terms of quantities on the 3-manifold. For instance, the connection coefficients $^{(4)}\Gamma^\lambda_{\mu\nu}$ associated with the four-dimensional metric are

$$\begin{aligned} ^{(4)}\Gamma^\lambda_{\mu\nu} &= {}^{(3)}\Gamma^\lambda_{\mu\nu} + \Omega^\lambda_{\mu\nu} \\ &= {}^{(3)}\Gamma^\lambda_{\mu\nu} + \tfrac{1}{2}s^2 g^{\lambda\sigma}[Y_\nu Z_{\mu\sigma} + Y_\mu Z_{\nu\sigma} - \partial_\sigma(\ln s^2)Y_\mu Y_\nu] + \tfrac{1}{2}Y^\lambda[\partial_\mu(s^2 Y_\nu) + \partial_\nu(s^2 Y_\mu)], \end{aligned} \tag{6}$$

where $^{(3)}\Gamma^\lambda_{\mu\nu}$ are the connection coefficients constructed from the 3-metric $g_{\mu\nu}$, and we have defined the antisymmetric tensor

$$Z_{\mu\nu} = \partial_\mu Y_\nu - \partial_\nu Y_\mu. \tag{7}$$

Note that $Z_{\mu\nu}$ is an intrinsically three-dimensional object, in that $Z_{\mu\nu}X^\mu = Z_{\mu\nu}X^\nu = 0$. With some algebra, the Ricci tensor on the 4-manifold, $^{(4)}R_{\mu\nu}$, can now be written as the Ricci tensor on the reduced space, $^{(3)}R_{\mu\nu}$, together with additional terms involving fields coming from the dimensional reduction

$$^{(4)}R_{\mu\nu} = {}^{(3)}R_{\mu\nu} + D_\lambda\Omega^\lambda_{\mu\nu} - D_\mu\Omega^\lambda_{\nu\lambda} + \Omega^\lambda_{\mu\nu}\Omega^\sigma_{\lambda\sigma} - \Omega^\sigma_{\mu\lambda}\Omega^\lambda_{\nu\sigma}, \tag{8}$$

where D_μ is the covariant derivative on the three-dimensional manifold. Expressed in terms of s, Y_a, Z_{ab} and $^{(3)}R_{ab}$, the components of (8) are

$$^{(4)}R_{\varphi\varphi} = \frac{1}{4}s^4 Z_{bc}Z^{bc} - sD^a D_a s, \tag{9}$$

$$^{(4)}R_{\varphi a} = \frac{1}{2s}D^c(s^3 Z_{ac}) + Y_a\left[\frac{1}{4}s^4 Z_{bc}Z^{bc} - sD^a D_a s\right], \tag{10}$$

$$\begin{aligned} ^{(4)}R_{ab} = {}^{(3)}R_{ab} &- \frac{1}{s}D_a D_b s - \frac{1}{2}s^2 Z_{ac}Z_b{}^c \\ &- \frac{1}{s}D^c[s^3 Z_{c(a}]Y_{b)} + Y_a Y_b\left[\frac{1}{4}s^4 Z_{bc}Z^{bc} - sD^a D_a s\right]. \end{aligned} \tag{11}$$

Taking the trace of (8), and using the definitions described above, gives the decomposition of the Ricci scalar as

$$^{(4)}R = {}^{(3)}R - \frac{2}{s}D^a D_a s - \frac{1}{4}s^2 Z_{bc}Z^{bc}. \tag{12}$$

The four-dimensional Einstein equations, with a stress–energy tensor $T_{\mu\nu}$, are

$$^{(4)}R_{\mu\nu} - \tfrac{1}{2}{}^{(4)}R\gamma_{\mu\nu} = 8\pi T_{\mu\nu}. \tag{13}$$

Using equations (9)–(12), we can write the Einstein equations as

$$D^a D_a s = -\frac{w_a w^a}{2s^3} - \frac{8\pi}{s}\left(T_{\varphi\varphi} - \frac{1}{2}s^2 T_\lambda{}^\lambda\right), \tag{14}$$

$$D_{[a}w_{b]} = 8\pi s\epsilon_{ab}{}^c T_{c\varphi}, \tag{15}$$

$$^{(3)}R_{ab} = \frac{1}{s}D_a D_b s + \frac{1}{2}s^2 Z_{ac}Z_b{}^c + 8\pi\left(T_{\mu\nu}g^\mu{}_a g^\nu{}_b - \frac{1}{2}g_{ab}T_\lambda{}^\lambda\right), \tag{16}$$

where we have introduced the twist w_μ of the Killing vector

$$w_\mu = \frac{s^4}{2} \epsilon_{\mu\nu\lambda\sigma} Y^\nu Z^{\lambda\sigma}, \tag{17}$$

and the four- and three-dimensional Levi-Civita symbols $\epsilon_{\mu\nu\lambda\sigma}$ and ϵ_{abc}, respectively. The twist vector w_μ is intrinsically three-dimensional, i.e. $w_\mu X^\mu = 0$. Furthermore, w_a/s^3 is divergence free

$$D^a \left[\frac{w_a}{s^3} \right] = 0. \tag{18}$$

At this point, the first reduction is essentially done. Equation (16) can be viewed as the three-dimensional Einstein equations, coupled to the projection of the stress–energy tensor $T_{\mu\nu}$ and to induced 'matter fields' s and w_a (or Z_{ab}). The equations of motion for s and w_a are given by (14) and (15) respectively; additional equations of motion will need to be specified for whatever true matter fields one incorporates into the system. This procedure so far is completely analogous to the Kaluza–Klein reduction from five to four dimensions, in which the five-dimensional geometry becomes gravity in four dimensions coupled to electromagnetism and a scalar field [27]. Here, however, the reduced 3-manifold has no dynamics and we have the rather appealing picture of having 'divided out' the dynamics of the four-dimensional gravitational system and reinterpreted the two degrees of freedom in the gravitational field as scalar (s) and 'electromagnetic' (Z_{ab}, or w_a) degrees of freedom[6].

We now perform the ADM split of the remaining spacetime. This is done by first foliating the three-dimensional spacetime into a series of spacelike hypersurfaces with unit, timelike normal vector n^a. Then, similar to the dimensional reduction above, we decompose quantities into components orthogonal and tangent to n^a, using the projection tensor h_{ab}

$$h_{ab} = g_{ab} + n_a n_b. \tag{19}$$

We now define the components of n^a, and the induced two-dimensional[7] metric h_{AB}, using the following decomposition of the 3-metric

$$g_{ab}\, \mathrm{d}x^a\, \mathrm{d}x^b = -\alpha^2\, \mathrm{d}t^2 + h_{AB}(\mathrm{d}x^A + \beta^A\, \mathrm{d}t)(\mathrm{d}x^B + \beta^B\, \mathrm{d}t), \tag{20}$$

where α is the lapse function and β^A the shift vector. The gravitational equations now become the evolution equations for the components of the 2-metric h_{AB} and the 2-extrinsic curvature K_{AB}

$$\partial_t h_{AB} = -2\alpha K_{AB} + \Delta_A \beta_B + \Delta_B \beta_A \tag{21}$$

$$\partial_t K_{AB} = \beta^C \Delta_C K_{AB} + K_{AC} \Delta_B \beta^C + K_{BC} \Delta_A \beta^C + \alpha[K K_{AB} + {}^{(2)}R_{AB}]$$
$$- 2\alpha K_{AC} K_B{}^C - \Delta_A \Delta_B \alpha - \alpha {}^{(3)}R_{AB}, \tag{22}$$

the Hamiltonian constraint equation

$${}^{(2)}R - K^A{}_B K^B{}_A + K^2 = {}^{(3)}R + 2{}^{(3)}R_{ab} n^a n^b \tag{23}$$

and the ρ and z momentum constraint equations

$$\Delta_A K_B{}^A - \Delta_A K = -{}^{(3)}R_{cd} n^d h^c{}_B. \tag{24}$$

In the above, Δ_A is the covariant derivative compatible with the 2-metric h_{AB}, $K \equiv K_A{}^A$, and ${}^{(2)}R_{AB}$ and ${}^{(2)}R$ are the two-dimensional Ricci tensor and Ricci scalar, respectively. Note that because gravity in three dimensions has no propagating degrees of freedom, the constraint

[6] Recall that the electromagnetic field in three dimensions has only a single degree of freedom as compared to the two degrees of freedom in four dimensions.

[7] We use upper-case Latin indices to denote two-dimensional tensor components.

equations fix the three-dimensional geometry completely. Thus, if desired, one can use the constraint equations (23), (24) instead of the evolution equations (21), (22) to solve for h_{AB}. The freely specifiable degrees of freedom of the 4-manifold are encoded in s and w_a, which are evolved using (14), (15) and (18). Note that (15) and (18) constitute four equations for the three components of w_a—the purely spatial have four equations for the three components of w_a. The purely spatial part of (15) is, in 3+1 language, the angular momentum constraint equation and only needs to be solved at the initial time in a free evolution of w_a. We note that the restricted class of axisymmetric spacetimes having no angular momentum (rotation) is characterized by the existence of a *scalar twist*, w, such that $w_a \equiv w_{,a}$. In the vacuum case, w generally represents odd parity gravitational waves, while s encodes even parity, or Brill waves. We further note that this class includes the special case $w_a \equiv 0$, which will be the focus of our discussion below.

3. Coordinate system, variables and equations

In this section we describe a particular coordinate system and set of variables which, in the context of the formalism described in the previous section, provides us with the concrete system of partial differential equations that we solve numerically. We also detail the outer boundary conditions we use, and the on-axis regularity conditions necessary to obtain smooth solutions to these equations.

We only consider spacetimes with zero angular momentum, and no odd-parity gravitational waves; therefore $w_a = 0$. We choose a conformally flat, cylindrical coordinate system for the 2-metric

$$h_{AB}\, \mathrm{d}x^A\, \mathrm{d}x^B = \psi(\rho, z, t)^4 (\mathrm{d}\rho^2 + \mathrm{d}z^2). \tag{25}$$

This choice for h_{AB} exhausts the coordinate freedom we have to arbitrarily specify the two components of the shift vector—$\beta^\rho(\rho, z, t)$ and $\beta^z(\rho, z, t)$. In order to maintain the form (25) during an evolution, we use the momentum constraints, which are elliptic equations, to solve for β^ρ and β^z at each timestep. The Hamiltonian constraint provides a third elliptic equation that we can use to solve for the conformal factor ψ. For a slicing condition, we use maximal slicing of $t = \text{const}$ hypersurfaces *in the four-dimensional manifold*—i.e. we impose $^{(3)}K = 0$, where $^{(3)}K$ is the trace of the extrinsic curvature tensor of $t = \text{const}$ slices of $\gamma_{\mu\nu}$. This condition (specifically $\partial^{(3)}K/\partial t = 0$) gives us an elliptic equation for the lapse.

Instead of directly evolving the norm of the Killing vector, s, we evolve the quantity $\bar{\sigma}$, defined by

$$s = \rho \psi^2 \, \mathrm{e}^{\rho \bar{\sigma}}, \tag{26}$$

and furthermore, we convert the resultant evolution equation for $\bar{\sigma}$ (14) to one that is first order in time by defining the quantity $\bar{\Omega}$, which is a 'conjugate' variable to $\bar{\sigma}$, via

$$\rho \bar{\Omega} = -2K_\rho{}^\rho - K_z{}^z$$
$$= -\frac{3}{2} n^a (\ln s)_{,a} + \frac{\beta^z_{,z} - \beta^\rho_{,\rho}}{2\alpha}. \tag{27}$$

Part of the motivation behind using $\bar{\sigma}$ and $\bar{\Omega}$ as fundamental variables is to simplify the enforcement of on-axis regularity. Regularity as $\rho \to 0$ implies that all variables exhibit either even or odd Taylor expansions in ρ. In particular, $\bar{\sigma}$ and $\bar{\Omega}$ must have leading order behaviour of the forms $\bar{\sigma} = \bar{\sigma}_1(z, t)\rho + O(\rho^3)$ and $\bar{\Omega} = \bar{\Omega}_1(z, t)\rho + O(\rho^3)$ respectively, and experience has shown it to be easier to enforce such conditions, than to enforce the leading order behaviour of s (or its time derivative) near the axis, which is $s = s_2(z, t)\rho^2 + O(\rho^4)$.

As mentioned previously, the only matter source we currently incorporate is a massless scalar field $\Phi(\rho, z, t)$, which satisfies the usual four-dimensional wave equation $\Box \Phi = 0$. We convert this equation to first-order-in-time form by defining a conjugate variable Π

$$\Pi \equiv \psi^2 n^a \Phi_{,a}. \tag{28}$$

The stress–energy tensor for the scalar field is

$$T_{\mu\nu} = 2\Phi_{,\mu}\Phi_{,\nu} - \gamma_{\mu\nu}\Phi^{,\mu}\Phi_{,\mu}, \tag{29}$$

and note that we are using a definition which differs from the usual scalar field stress–energy tensor by an overall factor of 2.

Using all of the above definitions and restrictions within the formalism detailed in the previous section, we end up with the following system of equations that we solve with our numerical code, described in the next section. The maximal slicing condition results in the following elliptic equation for α

$$2(\rho\alpha_{,\rho})_{,\rho^2} + \alpha_{,zz} + \alpha_{,\rho}\left(2\frac{\psi_{,\rho}}{\psi} + (\rho\bar\sigma)_{,\rho}\right) + \alpha_{,z}\left(2\frac{\psi_{,z}}{\psi} + (\rho\bar\sigma)_{,z}\right) - \frac{\psi^4}{2\alpha}\left[\left(\beta^\rho_{,\rho} - \beta^z_{,z}\right)^2\right.$$
$$\left. + \left(\beta^\rho_{,z} + \beta^z_{,\rho}\right)^2\right] - \frac{\psi^4}{6\alpha}\left[2\alpha\rho\bar\Omega + \beta^\rho_{,\rho} - \beta^z_{,z}\right]^2 = 16\pi\alpha\Pi^2, \tag{30}$$

where we have introduced the notation $f_{,\rho^2} \equiv \partial(f)/\partial(\rho^2)$. The Hamiltonian constraint gives an elliptic equation for ψ

$$8\frac{\psi_{,\rho\rho}}{\psi} + 8\frac{\psi_{,zz}}{\psi} + 16\frac{\psi_{,\rho^2}}{\psi} + 8(\rho\bar\sigma)_{,\rho}\frac{\psi_{,\rho}}{\psi} + 8(\rho\bar\sigma)_{,z}\frac{\psi_{,z}}{\psi} + \frac{\psi^4}{2\alpha^2}\left[\left(\beta^\rho_{,\rho} - \beta^z_{,z}\right)^2\right.$$
$$\left. + \left(\beta^\rho_{,z} + \beta^z_{,\rho}\right)^2\right] + \frac{\psi^4}{6\alpha^2}\left[2\alpha\rho\bar\Omega + \beta^\rho_{,\rho} - \beta^z_{,z}\right]^2$$
$$= -16\pi\left(\Pi^2 + \Phi_{,\rho}{}^2 + \Phi_{,z}{}^2\right) - 6(\rho^2(\rho\bar\sigma)_{,\rho})_{,\rho^3}$$
$$- 2((\rho\bar\sigma)_{,\rho})^2 - 2(\rho\bar\sigma)_{,zz} - 2((\rho\bar\sigma)_{,z})^2. \tag{31}$$

The ρ and z momentum constraints, which provide elliptic equations that we use to solve for β^ρ and β^z, are

$$\frac{2}{3}\beta^\rho_{,\rho\rho} + \beta^\rho_{,zz} + \frac{1}{3}\beta^z_{,z\rho} - \frac{2\alpha\rho}{3}\left[6\bar\Omega\frac{\psi_{,\rho}}{\psi} + \bar\Omega_{,\rho} + 3\bar\Omega(\rho\bar\sigma)_{,\rho}\right] - \frac{8}{3}\alpha\bar\Omega - \frac{2}{3}\left[\frac{\alpha_{,\rho}}{\alpha} - 6\frac{\psi_{,\rho}}{\psi}\right]$$
$$\times\left(\beta^\rho_{,\rho} - \beta^z_{,z}\right) - \left[\frac{\alpha_{,z}}{\alpha} - 6\frac{\psi_{,z}}{\psi} - (\rho\bar\sigma)_{,z}\right]\left(\beta^\rho_{,z} + \beta^z_{,\rho}\right)$$
$$= -32\pi\frac{\alpha}{\psi^2}\Pi_{,\rho}, \tag{32}$$

and

$$\beta^z_{,\rho\rho} + \frac{4}{3}\beta^z_{,zz} - \frac{1}{3}\beta^\rho_{,z\rho} - \frac{2\alpha\rho}{3}\left[6\bar\Omega\frac{\psi_{,z}}{\psi} + \bar\Omega_{,z} + 3\bar\Omega(\rho\bar\sigma)_{,z}\right]$$
$$+ \frac{4}{3}\left[\frac{\alpha_{,z}}{\alpha} - 6\frac{\psi_{,z}}{\psi} - \frac{3}{2}(\rho\bar\sigma)_{,z}\right]\left(\beta^\rho_{,\rho} - \beta^z_{,z}\right)$$
$$+ \left[\frac{2\alpha}{\psi^6}\left(\frac{\rho\psi^6}{\alpha}\right)_{,\rho^2} + (\rho\bar\sigma)_{,\rho}\right]\left(\beta^\rho_{,z} + \beta^z_{,\rho}\right) = -32\pi\frac{\alpha}{\psi^2}\Pi_{,z}. \tag{33}$$

The definition of $\bar\Omega$ in equation (27) gives an evolution equation for $\bar\sigma$ (where the overdot denotes partial differentiation with respect to t)

$$\dot{\bar\sigma} = 2\beta^\rho(\rho\bar\sigma)_{,\rho^2} + \beta^z\bar\sigma_{,z} - \alpha\bar\Omega - \left(\frac{\beta^\rho}{\rho}\right)_{,\rho}. \tag{34}$$

The evolution equation for $\bar{\Omega}$ is

$$\dot{\bar{\Omega}} = 2\beta^\rho(\rho\bar{\Omega})_{,\rho^2} + \beta^z\bar{\Omega}_{,z} - \frac{1}{2\alpha\rho}\left(\beta^z_{,\rho}{}^2 - \beta^\rho_{,z}{}^2\right) + \frac{1}{\psi^4}\left(\frac{\alpha_{,\rho}}{\rho}\right)_{,\rho}$$
$$+ \frac{\alpha}{\psi^6}\left(\frac{(\psi^2)_{,\rho}}{\rho}\right)_{,\rho} - \frac{2\alpha}{\psi^4}\left(4\frac{\psi_{,\rho^2}}{\psi} + (\rho\bar{\sigma})_{,\rho^2}\right)\left(\frac{\alpha_{,\rho}}{\alpha} + \frac{2\psi_{,\rho}}{\psi}\right)$$
$$- \frac{\alpha}{\psi^4}\left[\bar{\sigma}_{,z}\left(\frac{\alpha_{,z}}{\alpha} + \frac{2\psi_{,z}}{\psi}\right) + \rho\bar{\sigma}_{,z}{}^2 + \bar{\sigma}_{,zz}\right] + 64\pi\frac{\alpha}{\psi^4}\rho(\Phi_{,\rho^2})^2. \tag{35}$$

We also have an evolution equation for ψ, which we optionally use instead of the Hamiltonian constraint (31) to update ψ

$$\dot{\psi} = \psi_{,z}\beta^z + \psi_{,\rho}\beta^\rho + \frac{\psi}{6}\left(2\beta^\rho_{,\rho} + \beta^z_{,z} + \rho\alpha\bar{\Omega}\right). \tag{36}$$

The definition of Π and the wave equation for Φ give

$$\dot{\Phi} = \beta^\rho\Phi_\rho + \beta^z\Phi_z + \frac{\alpha}{\psi^2}\Pi, \tag{37}$$

and

$$\dot{\Pi} = \beta^\rho\Pi_{,\rho} + \beta^z\Pi_{,z} + \frac{1}{3}\Pi\left(\alpha\rho\bar{\Omega} + 2\beta^\rho_{,\rho} + \beta^z_{,z}\right) + \frac{1}{\psi^4}\left[2(\rho\alpha\psi^2\Phi_\rho)_{,\rho^2} + (\alpha\psi^2\Phi_z)_{,z}\right]$$
$$+ \frac{\alpha}{\psi^2}\left[(\rho\bar{\sigma})_{,\rho}\Phi_\rho + (\rho\bar{\sigma})_{,z}\Phi_z\right]. \tag{38}$$

To complete the specification of our system of equations, we need to supply boundary conditions. In our cylindrical coordinate system, where ρ ranges from $\rho = 0$ to $\rho = \rho_{max}$ and z ranges from z_{min} to z_{max}, we have two distinct boundaries: the physical outer boundary at $\rho = \rho_{max}, z = z_{min}$ and $z = z_{max}$; and the axis, at $\rho = 0$. Historically, the axis presented a stability problem in axisymmetric codes. We solve this problem by enforcing regularity on the axis, and, as described in section 5, adding numerical dissipation to evolved fields.

The regularity conditions can be obtained by inspection of the equations in the limit $\rho \to 0$, or more formally, by transforming to Cartesian coordinates and demanding that components of the metric and matter fields be regular and single valued throughout [26]. Garfinkle and Duncan [14] have further proposed that in order to ensure smoothness on the axis, one should use quantities that have either even or odd power series expansions in ρ as $\rho \to 0$, but which do not vanish faster than $O(\rho)$. It is interesting that the quantities which we found to work best also obey this requirement. As discussed earlier, the particular choice of $\bar{\sigma}$ and $\bar{\Omega}$ as fundamental variables was partly motivated by regularity concerns. The results are

$$\alpha_{,\rho}(0, z, t) = 0 \tag{39}$$
$$\psi_{,\rho}(0, z, t) = 0 \tag{40}$$
$$\beta^z_{,\rho}(0, z, t) = 0 \tag{41}$$
$$\beta^\rho(0, z, t) = 0 \tag{42}$$
$$\bar{\sigma}(0, z, t) = 0 \tag{43}$$
$$\bar{\Omega}(0, z, t) = 0 \tag{44}$$
$$\Phi_{,\rho}(0, z, t) = 0 \tag{45}$$
$$\Pi_{,\rho}(0, z, t) = 0. \tag{46}$$

At the outer boundary, we enforce asymptotic flatness by requiring

$$\lim_{r \to \infty} \alpha(r, t) = 1 + \frac{C(t)}{r} + O(r^{-2}) \tag{47}$$

$$\lim_{r \to \infty} \psi(r, t) = 1 + \frac{D(t)}{r} + O(r^{-2}) \tag{48}$$

$$\lim_{r \to \infty} \beta^z(r, t) = \frac{E(t)}{r} + O(r^{-2}) \tag{49}$$

$$\lim_{r \to \infty} \beta^\rho(r, t) = \frac{F(t)}{r} + O(r^{-2}), \tag{50}$$

for undetermined functions $C(t)$, $D(t)$, $E(t)$, $F(t)$ and $r^2 \equiv \rho^2 + z^2$. These latter relations are converted to mixed (Robin) boundary conditions (see appendix A for details) and then are imposed at the outer boundaries of the computational domain: $\rho = \rho_{max}$, $z = z_{max}$ and $z = -z_{max}$. We have also experimented with the use of Dirichlet conditions on α, β^ρ and β^z at the outer boundaries (specifically $\alpha = 1$ and $\beta^\rho = \beta^z = 0$ there), and have found that these work about as well as the Robin conditions. For the scalar field, we assume that near the outer boundary we can approximate the field as purely radially outgoing, and require

$$(r\Phi)_{,t} + (r\Phi)_{,r} = 0. \tag{51}$$

For scalar field configurations far from spherical symmetry, this approximation suffers and reflections are relatively large. However, in general, the reflections do not grow and are somewhat damped. For the other two evolved quantities, $\bar{\sigma}$ and $\bar{\Omega}$, we use this same naive condition for lack of any better, more physically motivated conditions. While this condition proves to be stable with damped reflections, a better condition is sought and this issue remains under investigation.

For initial conditions, we are free to set $(\bar{\sigma}(0, \rho, z), \bar{\Omega}(0, \rho, z), \Phi(0, \rho, z), \Pi(0, \rho, z))$. Once the free data are chosen, we then use the constraint and slicing equations to determine $(\alpha(0, \rho, z), \psi(0, \rho, z), \beta^z(0, \rho, z), \beta^\rho(0, \rho, z))$. Specifically, we define a general pulse shape

$$G_X(\rho, z) = A_X \exp\left[-\left(\frac{\sqrt{(\rho - \rho_X)^2 + \epsilon_X (z - z_X)^2} - R_X}{\Delta_X} \right)^2 \right] \tag{52}$$

characterized by six parameters $(A_x, \rho_X, \epsilon_X, z_X, R_X, \Delta_X)$ and then choose initial data of the form

$$\begin{aligned} \bar{\sigma}(0, \rho, z) &= \rho G_{\bar{\sigma}}(\rho, z) \\ \bar{\Omega}(0, \rho, z) &= \rho G_{\bar{\Omega}}(\rho, z) \\ \Phi(0, \rho, z) &= G_\Phi(\rho, z) \\ \Pi(0, \rho, z) &= 0. \end{aligned} \tag{53}$$

For $\epsilon_X = 1$, these pulses are Gaussian, spherical shells centred at (ρ_X, z_X) with radius R_X and pulse width Δ_X. For $\epsilon_X = 1$ and $(\rho_X, z_X) = (0, 0)$, the pulses are spherical. The factor of ρ in the initial data for $\bar{\sigma}$ and $\bar{\Omega}$ ensures the correct behaviour on axis for regularity. We also note that when $\rho_X \neq 0$, G_X is not formally an even function of ρ; in such cases, we always set $\rho_X \gg \Delta_X$ so that $G_X(0, z) \approx 0$, and to well within the precision of our computations, the regularity condition on G_X *is* satisfied at the initial time. For the evolutions presented here, we set $\Pi(0, \rho, z) = \bar{\Omega}(0, \rho, z) = 0$, so that the initial configurations represent moments of time symmetry. We note, however, that we are also able to generate and evolve approximately ingoing initial data for the scalar field.

4. Finding apparent horizons

In this section, we describe the equation and technique we use to search for apparent horizons (AHs) within $t = \text{const}$ spatial slices of the spacetime (see [7, 28, 29] for descriptions of some of the methods available to find AHs in axisymmetry). We restrict our search to isolated, simply connected AHs. In axisymmetry, such an AH can be described by a curve in the (ρ, z) plane, starting and ending on the axis at $\rho = 0$. We define the location of the AH as the level surface $F = 0$, where

$$F = \bar{r} - R(\bar{\theta}), \tag{54}$$

and

$$\bar{r} \equiv \sqrt{\rho^2 + (z - z_0)^2}, \tag{55}$$

$$\bar{r} \sin \bar{\theta} \equiv \rho, \tag{56}$$

$$\bar{r} \cos \bar{\theta} \equiv (z - z_0). \tag{57}$$

The AH is the outermost, marginally trapped surface; hence, we want to find an equation for $R(\bar{\theta})$ such that the outward null expansion normal to the surface $F = 0$, is zero. To this end, we first construct the unit spatial vector s^a, normal to $F = \text{const}$

$$s^a = \frac{g^{ab} F_{,b}}{\sqrt{g^{cd} F_{,c} F_{,d}}}. \tag{58}$$

Then, using s^a and the $t = \text{const}$ hypersurface normal vector n^a, we construct future-pointing outgoing $(+)$ and ingoing $(-)$ null vectors as

$$\ell_{\pm}^a = n^a \pm s^a. \tag{59}$$

The normalization of the null vectors is (arbitrarily) $\ell_+^a \ell_{-a} = -2$. The outward null expansion θ_+ is then the divergence of ℓ_+^a projected onto $F = \text{const}$

$$\theta_+ = (g^{ab} - s^a s^b) \nabla_b \ell_{+a}. \tag{60}$$

Using the definition of the extrinsic curvature K_{AB}, and substituting (59) into (60), we arrive at the familiar form for the null expansion when written in terms of ADM variables

$$\theta_+ = s^A s^A K_{AB} + \Delta_A s^A - K. \tag{61}$$

Note that because the normalization of ℓ_+^a is arbitrary, so (to some extent) is that of θ_+. The above normalization is chosen so that θ_+ measures the fractional rate of change of area with time measured by an observer moving along n^a.

Substituting (54) and (58) into (61), and setting $\theta_+ = 0$, we are left with an ordinary differential equation for $R(\bar{\theta})$. This equation takes the following form, where a prime $'$ denotes differentiation with respect to $\bar{\theta}$

$$R''(\bar{\theta}) + G(R'(\bar{\theta}), R(\bar{\theta}), g_{ab}, g_{ab,\rho}, g_{ab,z}) = 0. \tag{62}$$

G is a rather lengthy function of its arguments, nonlinear in R and R'; for brevity we do not display it explicitly. All of the metric functions and their gradients appearing in (62) are evaluated along a given curve of integration, and hence are implicitly functions of $\bar{\theta}$. $\bar{\theta}$ ranges from 0 to π, and regularity of the surface $F = 0$ about the axis requires $R'(0) = R'(\pi) = 0$. Integration of (62) therefore proceeds by specifying R at $\bar{\theta} = 0$ (for instance), and then 'evolving' R until either $\bar{\theta} = \pi$, or R diverges at some value of $\bar{\theta} < \pi$. If an AH exists, and

assuming z_0 is inside the AH, then the AH can be found by searching for the (locally) unique[8] initial value $R(0) = R_0$ such that integration of (62) ends at $R(\pi) = R_\pi$, with $R'(\pi) = 0$ and R_π finite. For $R(0)$ slightly larger than R_0 (outside the AH), the integration will end at $\bar\theta = \pi$ with $R'(\pi) > 0$, indicating an irregular point on the surface; similarly, for $R(0)$ slightly smaller than R_0 (inside the AH) the integration will end with $R'(\pi) < 0$. Therefore, if we can find a reasonable bracket about the unknown R_0, we can use a bisection search to find R_0. Currently, we find a bracket to search by testing a set of initial points, equally spaced in z at intervals of $3\Delta z$. This seems to work well in most situations, and the search is reasonably fast.

We use a second-order Runge–Kutta method to integrate equation (62). The metric functions appearing in G are evaluated using bilinear interpolation along the curve.

5. Implementation

In this section we describe the numerical code that we have written to solve the equations listed in section 3. Some details are deferred to appendix A.

We use a uniform grid of size N_ρ points in ρ by N_z points in z, with equal spacing $\Delta\rho = \Delta z = h$ in the ρ and z directions. The value of a function f at time level n and location (i, j) within the grid, corresponding to coordinate $(\rho, z, t) = ((i - 1)\Delta\rho, (j - 1)\Delta_z + z_{\min}, n\Delta t)$, is denoted by $f_{i,j}^n$. For the temporal discretization scale we use $\Delta t = \lambda h$, where λ is the Courant factor, which for the type of differencing we employ, should be less than one for stability; typically we use $\lambda = 0.3$. The hyperbolic equations (34)–(38) are discretized using a second-order accurate Crank–Nicholson-type scheme, whereby we define two time levels, t and $t + \Delta t$, and obtain our finite difference stencils by expanding in Taylor series about $t = t + \Delta t/2$. This gives the following second-order accurate approximation to the first derivative of f with respect to time

$$\frac{f_{i,j}^{n+1} - f_{i,j}^n}{\Delta t} = \left.\frac{\partial f(\rho, z, t)}{\partial t}\right|_{t=t+\Delta t/2} + O(\Delta t^2). \tag{63}$$

Second-order accurate approximations to functions and spatial derivative operators at $t = t + \Delta t/2$ are obtained by averaging the corresponding quantity, Q, in time

$$\frac{Q_{i,j}^n + Q_{i,j}^{n+1}}{2} = Q(t + \Delta t/2, \rho, z) + O(\Delta t^2). \tag{64}$$

Thus, after discretization of the evolution equations using (63) and (64), function values are only referenced at times t and $t + \Delta t$, even though the stencils are centred at time $t + \Delta t/2$. Specific forms for all the finite difference stencils that we use can be found in appendix A.

We add Kreiss–Oliger dissipation [30] to the evolution of equations of Φ, Π, $\bar\sigma$ and $\bar\Omega$ (in addition to ψ during partially constrained evolution), as described in appendix A. To demonstrate that this is *essential* for the stability of our numerical scheme, we compare in figure 1 the evolution of $\bar\sigma$ from simulations without and with dissipation, but otherwise identical.

The elliptic equations (30)–(33) are solved using Brandt's FAS multigrid (MG) algorithm [32, 33], described in some detail in appendix A. There are no explicit time derivatives of functions in these equations, and we discretize them at a single time level n (i.e. we do not apply the Crank–Nicholson averaging scheme for the elliptics). We use either a fully constrained evolution, solving for α, β^ρ, β^z and ψ using the constraint equations and slicing condition, or a partially constrained evolution where instead of using the Hamiltonian

---

[8] In a general collapse scenario, multiple inner horizons could be present, which would also satisfy (62) augmented with the conditions $R'(0) = R'(\pi) = 0$. We want the outermost of these surfaces.
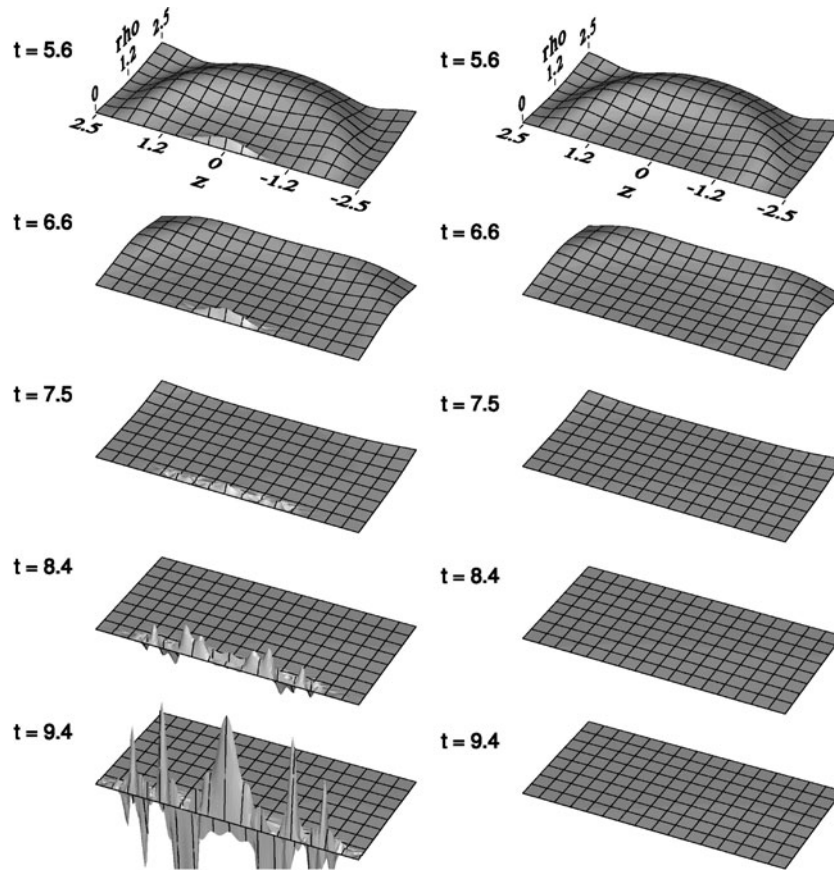
Figure 1. The metric variable $\bar{\sigma}$ from two sample Brill wave evolutions, demonstrating the effectiveness of dissipation. Both simulations were run with identical parameters, except the simulation displayed on the left was run without dissipation, while that shown on the right was run with a dissipation parameter $\epsilon = 0.5$ (see appendix A). The simulation without dissipation crashed at around $t = 10$, while the run with dissipation was stopped after several light crossing times, without showing any signs of instability. (Note: the computational domain used for these evolutions was $\rho = [0, 10]$, and $z = [-10, 10]$; in the plots above we only show a subset of this domain. Also, the grid lines drawn are for visual aid only; the size of the mesh visible in each frame is 64×128.)

constraint to update ψ, we use the evolution equation (36). Partially constrained evolution has proven to be useful due to the occasional failure of the MG solver in the strong-field regime (i.e. close to black-hole formation). Use of the evolution equation for ψ (rather than the Hamiltonian constraint) circumvents this problem in many instances; however, in certain Brill-wave dominated spacetimes, free evolution of ψ is not sufficient to ensure convergence of the MG process. We are currently working to make the MG solver more robust in these situations.

The code is written in a combination of RNPL (Rapid Numerical Prototyping Language [31]) and Fortran 77. The hyperbolic equations are implemented in RNPL, which employs a pointwise Newton–Gauss–Seidel iterative relaxation scheme to solve these equations, while the MG solver is implemented in Fortran (see appendix A for more MG details). A pseudo-code description of the time-stepping algorithm used is as follows:

```
a) As an initial guess to the solution at time t + dt, copy variables from
   t to t+dt
b) repeat until (residual norm < tolerance):
     1 : perform 1 Newton−Gauss−Seidel relaxation sweep of the evolution
         equations, solving for the unknowns at time t + dt
     2 : perform 1 MG vcycle on the set of elliptic equations, discretized
         at time t + dt
   end repeat
```

Note that during the Crank–Nicholson phase of the iteration (step 1), the elliptic variables at time $t + \mathrm{d}t$ are held fixed and treated as known functions; conversely, during the vcycle phase (step 2), the non-elliptic variables at time $t + \mathrm{d}t$ are treated as known functions. For the residual norm used to terminate the iteration we use the infinity norm of the residuals of all unknowns. Thus, after the iteration is complete, we have a set of variables at times t and $t + \mathrm{d}t$ that satisfy the hyperbolic difference equations at time $t + \mathrm{d}t/2$, and the elliptic difference equations at time $t + \mathrm{d}t$ (and time t from the solution obtained at the previous timestep, or initial time if $t = 0$) to within the desired tolerance.

6. Tests

In this section, we describe some of the tests we have performed to check that we are solving the correct set of equations. The first test consists of checking the equations against those derived with a computer algebra system[9]. By inputting the metric and coordinate conditions, the computer-derived equations can then be subtracted from our equations and simplified. By finding that the differences simplify to 0, we can conclude that two sets of equations agree.

For diagnostic purposes and as tests of the equations and of their discretization, we compute several quantities during the numerical evolution. The first is the ADM mass [25]

$$M_{\mathrm{ADM}} = \frac{1}{16\pi} \lim_{r \to \infty} \int \left(H^a{}_{b;a} - H^a{}_{a;b} \right) N^b \, \mathrm{d}A, \qquad (65)$$

where the integral is evaluated on a flat 3-space, i.e. with metric $\mathrm{d}s^2 = \mathrm{d}\rho^2 + \mathrm{d}z^2 + \rho^2 \, \mathrm{d}\phi^2$. The spatial 3-metric H_{ab} is that from our curved space solution, but has its indices raised and lowered with the flat metric. Integrating around the boundaries of our numerical grid, the normal vectors $\vec{N}$ are $\pm\partial/\partial z$ and $\partial/\partial\rho$. After some algebra, the ADM mass becomes

$$M_{\mathrm{ADM}} = \frac{1}{2} \int_{z_{\max}} \rho\psi^4 \left[-\frac{\psi_{,z}}{\psi} - \mathrm{e}^{2\rho\bar{\sigma}} \left(\frac{\psi_{,z}}{\psi} + \frac{1}{2}(\rho\bar{\sigma})_{,z} \right) \right] \mathrm{d}\rho$$

$$- \frac{1}{2} \int_{z_{\min}} \rho\psi^4 \left[-\frac{\psi_{,z}}{\psi} - \mathrm{e}^{2\sigma} \left(\frac{\psi_{,z}}{\psi} + \frac{1}{2}(\rho\bar{\sigma})_{,z} \right) \right] \mathrm{d}\rho$$

$$+ \frac{1}{2} \int_{\rho_{\max}} \rho\psi^4 \left[-\frac{\psi_{,\rho}}{\psi} - \mathrm{e}^{2\sigma} \left(\frac{\psi_{,\rho}}{\psi} + \frac{1}{2}(\rho\bar{\sigma})_{,\rho} + \frac{1}{4\rho} \right) + \frac{1}{4\rho} \right] \mathrm{d}z. \qquad (66)$$

A second set of quantities we calculate are the ℓ_2-norms of the residuals of the evolution equations for the extrinsic curvature (22), which we denote by $E(\dot{K}_{AB})$. Because we do not directly evolve individual components of the extrinsic curvature, these residuals will not be zero; however, they *should* converge to zero in the limits as the discretization scale $h \to 0$, and the outer boundary positions $\rho_{\max}, z_{\max}, -z_{\min} \to \infty$. Note that we include these last

---

[9] We use Waterloo Maple along with a tensor package written by one of the authors (MWC).
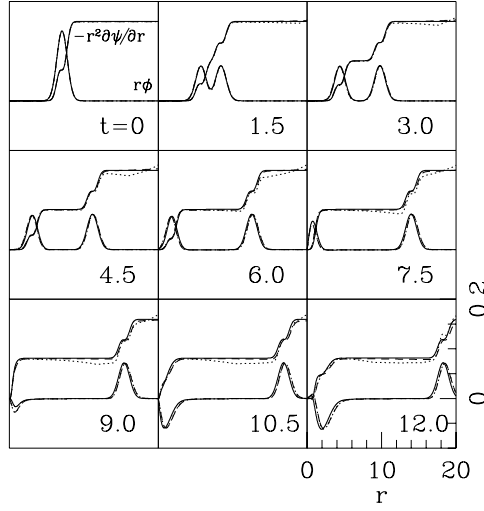
Figure 2. Tests of spherically symmetric scalar collapse. The sequence of frames are from the evolution of an initial pulse in Φ of the form (52) with $A_\Phi = 0.02$, $\epsilon_\Phi = 1$, $R_\Phi = 7.0$, $\Delta_\Phi = 1.0$, $(\rho_\Phi, z_\Phi) = (0, 0)$. Shown are the functions $r\Phi$ and $-r^2 \partial\psi/\partial r$. The output of the explicitly spherically symmetric code (with 2^{10} radial grid points) is shown with solid curves, while the output of the axisymmetric code ($N_\rho = N_z/2 = 2^8$) is shown with dashed (a $(\rho = 0, z > 0)$ slice) and dotted curves (a $z = 0$ slice).

conditions because it is only in the limit $r \to \infty$ that our outer boundary conditions are fully consistent with asymptotic flatness.

The convergence properties of our code are measured by computing the convergence factor, Q_u, associated with a given variable, u, obtained on grids with resolution h, $2h$ and $4h$ via

$$Q_u = \frac{\|u_{4h} - u_{2h}\|_2}{\|u_{2h} - u_h\|_2}. \tag{67}$$

In particular, for the case of $O(h^2)$ (second order) convergence, we expect $Q_u \to 4$ as $h \to 0$.

The first set of tests we present here are comparisons of Φ and ψ from the evolution of spherically symmetric initial data to the corresponding functions computed by a 1D spherically symmetric code, the details of which are presented in appendix B. In general, the results from the two codes are in good agreement. A sample comparison is illustrated in figure 2 which shows the scalar field obtained with the 1D code as well as two radial slices of the corresponding solution calculated using the axisymmetric code. Note, however, that we do not expect *exact* agreement in the limit $h \to 0$ for a fixed outer boundary location, as the 'rectangular' boundaries of the axisymmetric code are, in general, incompatible with precise spherical symmetry.

In the second series of tests, we examine evolutions of Brill waves and non-spherical scalar pulses. Figures 3–6 show results from two typical initial datasets, each computed using two distinct outer boundary positions. Each figure plots (a) the ADM mass M_{ADM}, (b) the ℓ_2-norm of the residual of the $\rho\rho$ component of the evolution equation for the extrinsic curvature $E(\dot{K}_{\rho\rho})$, and, (c) the convergence factor Q_ψ of ψ, as functions of time (the convergence factor Q for other functions exhibits similar behaviour as Q_ψ, and so for brevity we do not show them). Here, one expects to see an improvement of the results—namely trends towards mass conservation early on, a zero residual, and a convergence factor of 4—in the limits $h \to 0$
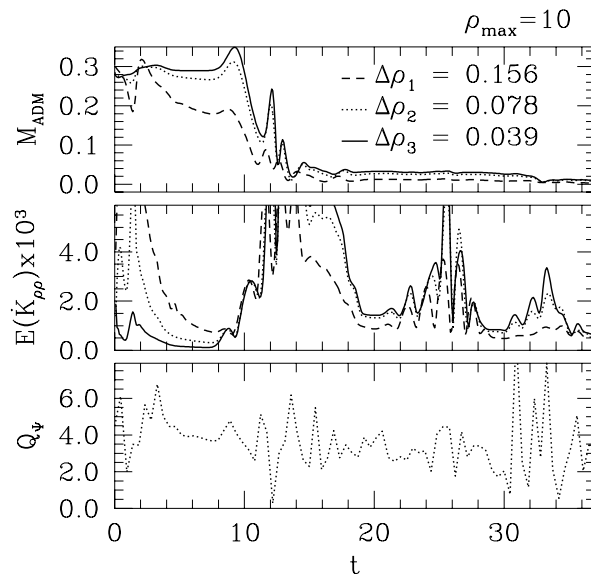
Figure 3. Tests of Brill collapse using a initial pulse profile for $\bar{\sigma}(0, \rho, z)$ of the form (52) with $A_{\bar{\sigma}} = -3.0$, $R_{\bar{\sigma}} = 0$, $\Delta_{\bar{\sigma}} = 1$, $\epsilon_{\bar{\sigma}} = 1$, and $(\rho_{\bar{\sigma}}, z_{\bar{\sigma}}) = (0, 0)$. The evolution shown here corresponds to four crossing times and $\rho_{max} = z_{max} = 10$. The top frame shows the calculated ADM mass M_{ADM}. As the resolution increases, so does the level of mass conservation at early times, before energy has reached the outer boundary. The middle frame shows $E(\dot{K}_{\rho\rho})$, the ℓ_2-norm of the residual of the $\rho\rho$ component of the evolution equation for the extrinsic curvature (22). At early times, before energy reaches the outer boundary, the residual decreases as the resolution increases. The bottom frame shows the convergence factor computed for the field ψ.
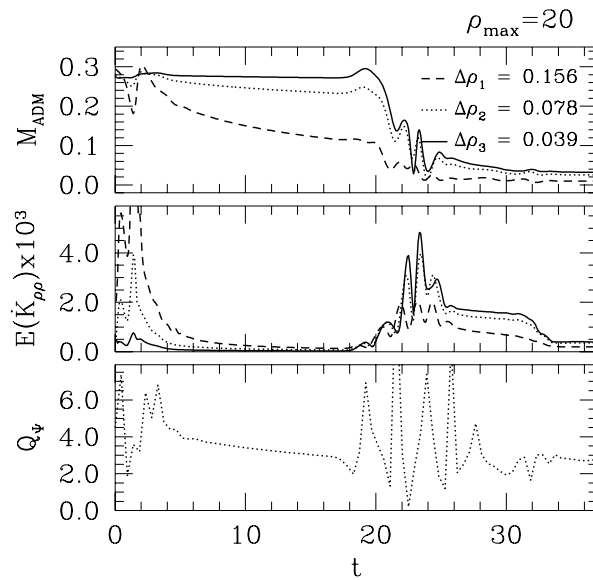
Figure 4. Tests of Brill collapse with the same initial data and grid resolutions as those in figure 3, but with $\rho_{max} = z_{max} = 20$, and for only two crossing times. Note the improvement in the behaviour of the residual and mass aspect when energy reaches the outer boundary, as compared to the $\rho_{max} = z_{max} = 10$ case above.
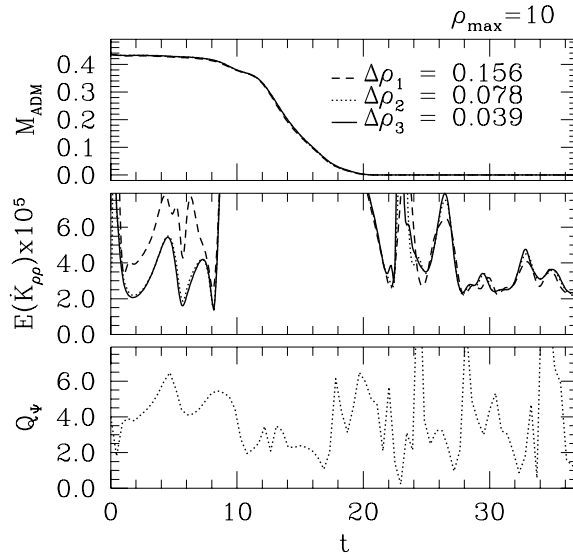
Figure 5. Tests of an oblate, scalar pulse evolution with $A_\Phi = 0.15$, $R_\Phi = 0$, $\Delta_\Phi = 3$ $\epsilon_\Phi = 3$ and $(\rho_\Phi, z_\Phi) = (0, 0)$. The tests are shown for four crossing times with $\rho_{max} = z_{max} = 10$. The results are similar to the tests for the Brill wave shown in figure 3, though note that the scale of the residual $E(\dot{K}_{\rho\rho})$ is about two orders of magnitude smaller than that of the Brill wave case.
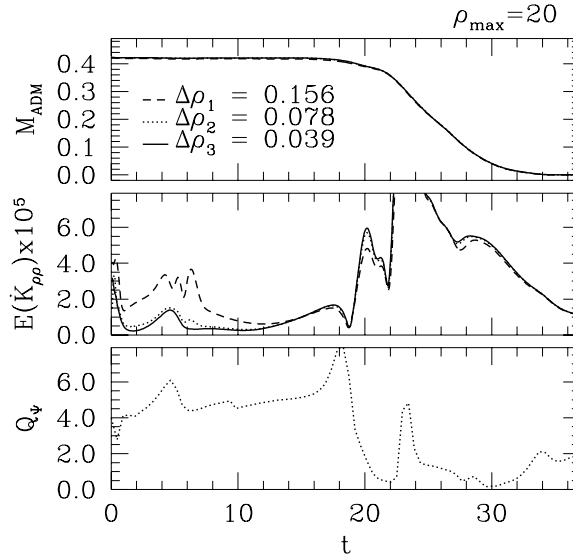
Figure 6. Tests of an oblate, scalar pulse evolution with the same initial data and grid resolutions as those in figure 5, but with $\rho_{max} = z_{max} = 20$, and for two crossing times. Again, as with the Brill wave example, it is evident that there are two factors that contribute to a non-zero residual $E(\dot{K}_{\rho\rho})$—the closeness of the outer boundary, and the discretization scale h.

and $(\rho_{max}, z_{max}) \to \infty$. After energy has reached the outer boundary, and to a lesser extent before (as is evident in the scalar field example in figures 5 and 6), we fail to get consistency with the evolution equation (22) as $h \to 0$, for *fixed* (ρ_{max}, z_{max}). This is a measure of the
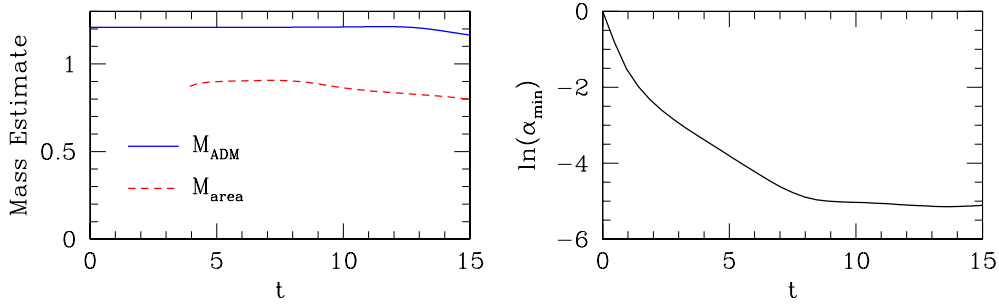
Figure 7. The ADM mass estimate M_{ADM} of the spacetime and area–mass estimate $M_{area} = \sqrt{A/16}$ of the black hole (left), where A is the area of the apparent horizon, and the natural logarithm of the minimum value of lapse (right) during a scalar field collapse simulation. The initial scalar field profile, $\Phi(0, \rho, z)$ is of the form (52) with $A_\Phi = 0.35$, $R_\Phi = 0$, $\Delta_\Phi = 1$, $\epsilon_\Phi = 1$ and $(\rho_\Phi, z_\Phi) = (0, 0)$. The outer boundary is at $\rho_{max} = z_{max} = -z_{min} = 10$, and the size of the numerical grid is 256×512. An apparent horizon was first detected at $t \approx 4$, hence the M_{area} curve only starts then. At intermediate times (between roughly $t = 2$ and $t = 7$) we see an exponential 'collapse' of the lapse (the minimum of which is at $(\rho, z) = (0, 0)$); at later times this behaviour ceases in the simulation, as a consequence of increasingly poor resolution in the vicinity of the black hole caused by 'grid-stretching'—see figure 8. This also adversely affects the accuracy of the area–mass estimate (it actually begins to *decrease* at late times) as the coordinate region occupied by the AH shrinks.

inaccuracy of our outer boundary conditions (47)–(50); though the trends suggest that we *do* achieve consistency in the limit $(\rho_{max}, z_{max}) \to \infty$.

Finally, we show some results of a simulation of black-hole formation from the collapse of a spherically symmetric distribution of scalar field energy. Again, by looking at spherically symmetric collapse we can compare with the 1D code (obtaining the same level of agreement as seen in the example in figure 2). However, here we want to show the behaviour of our coordinate system (in particular the maximal slicing) in the strong-field regime, which demonstrates the need to incorporate black-hole excision techniques and/or adaptive mesh refinement (AMR) before attempting any serious investigation of physics with this code. Figure 7 shows plots of the ADM mass estimate (65), an estimate of the black-hole mass $M_{area} \equiv \sqrt{A/16\pi}$, where A is the area of the apparent horizon, and the minimum value of the lapse as a function of time from the simulation. Figure 8 shows the conformal factor ψ at several times, in the central region of the grid.

Maximal slicing is considered *singularity avoiding* because, as the singularity is approached in a collapse scenario, the lapse α tends to 0, as demonstrated in figure 7. This effectively freezes the evolution inside the black hole, though it causes a severe distortion in the $t = $ const slices as one moves away from the black hole. This particular coordinate pathology is evident in figure 8. Recall from the 2-metric (25) that ψ^2 determines proper length scales in the ρ and z directions; thus the rapid growth with time of ψ shown in figure 8 means that a given coordinate area represents increasing proper area. Furthermore, the increase in magnitude of ψ in the strong-field regime (which happens even when black holes do not form, and in non-spherical scalar field and Brill wave evolution, though not to the same extent as shown in figure 8) implies that our effective numerical resolution decreases in those regions, as some feature of the solution with a given characteristic size will span less of the coordinate grid. Thus, in the end, even though maximal slicing may prevent us from reaching a physical singularity, the 'grid-stretching' effect is just as disastrous for the numerical code, preventing any long-term simulation of black-hole spacetimes. For these reasons we will add black-hole
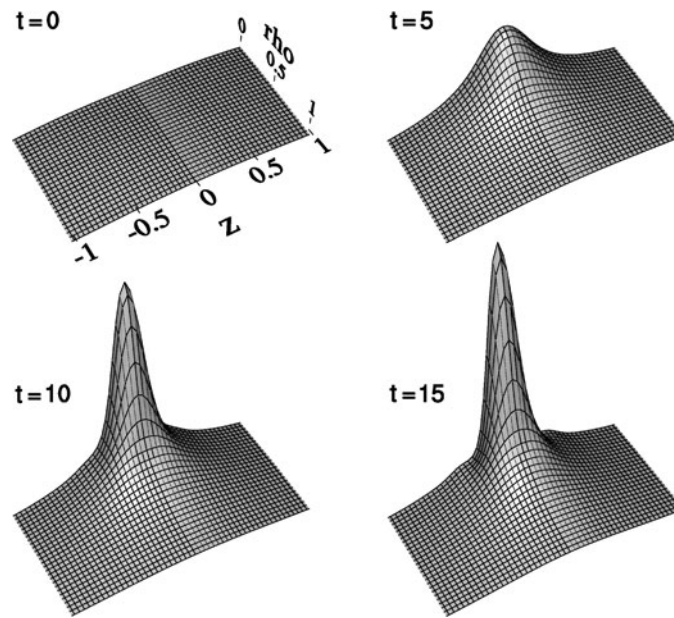
Figure 8. The conformal factor ψ near the origin, at four different times from the simulation described in figure 7. The height of the surfaces represents the magnitude of ψ, and the scale of each image is the same. The smallest value of ψ shown in each frame is ≈ 1.5, while at $t = 15$, ψ reaches a maximum of ≈ 5.8 at the origin. The 2-metric has the form $\psi^4(\mathrm{d}\rho^2 + \mathrm{d}z^2)$, hence the larger ψ is, the larger the physical area represented by a given coordinate cell (the lines drawn here *are* coincident with the actual grid lines of the simulation). This implies that the effective resolution of a given coordinate patch *decreases* as ψ increases. The net result is that as gravitational collapse proceeds, central features of the solution become very poorly resolved within the grid, adversely affecting the accuracy of the solution. This is quite evident at $t = 15$, where noticeable asymmetries have developed in ψ (recall that this is collapse from spherically symmetric initial data).

excision techniques and AMR before exploring physics with this code; our efforts in this regard are well underway, and will be described elsewhere.

7. Conclusion

We have described a (2+1)+1 gravitational evolution model which evolves axisymmetric configurations of gravitational radiation and/or a scalar field. A thorough battery of tests confirms that the correct equations are being solved. In particular, we have provided evidence that the code is second-order convergent, consistent and conserves mass in the limit where the outer boundary position goes to infinity. Furthermore, we have shown that using proper regularity conditions on the axis for all variables, together with adding dissipation to hyperbolic equations, removes related stability problems. This is similar to what was found by Garfinkle and Duncan [14] in their axisymmetric code, although we note that in contrast to that work, our discrete domain includes gridpoints *on* the z-axis. The 'Cartoon' method presented in [15], and used successfully in [10, 11], offers a completely different approach to stabilizing the axis, by effectively evolving a slab of a Cartesian grid. All of these works demonstrate that it is not an insurmountable problem to create stable codes that address a wide range of physical problems in axisymmetry.

The unigrid code described here is the first step towards our long-term goal of studying a range of interesting theoretical and astrophysical phenomena in axisymmetry. These include gravitational collapse of various matter sources and gravitational waves, the corresponding critical phenomena at the threshold of black-hole formation, head-on black-hole collisions and accretion disks. To this end, we need to include support for angular momentum and additional matter fields in the code, as well as to add additional computational and mathematical infrastructure—adaptive mesh refinement, black-hole excision and the capability of running in parallel on a network of machines. All of these projects are under development, and results will be published as they become available.

Another goal of this project is to provide a platform from which to develop computational technology for 3D work. In particular, we see development of AMR in axisymmetry as a precursor to its incorporation in 3D calculations. Likewise, accurate and stable treatment of boundary conditions presents a continual challenge in numerical relativity, and it is possible that we can develop an effective treatment of boundaries in axisymmetry that will generalize to the 3D case.

Acknowledgments

Appendix A. The elliptic solver and finite difference approximations

In this appendix we briefly mention some aspects of our multigrid (MG) routine, and list the set of finite difference approximations that we use.

The constraint equations (30)–(33) are four elliptic equations which, for a fully constrained system, must be solved on every time slice (i.e. spatial hypersurface). As such, it can be expected that the time taken by a given evolution will be dominated by the elliptic solver and hence we look for the fastest possible solver.

Currently, multigrid methods are among the most efficient elliptic solvers available, and here we have implemented a standard full approximation storage (FAS) multigrid method with V-cycling (see [32, 33]) to solve the four nonlinear equations simultaneously. (When using the evolution equation for ψ in a partially constrained evolution, we use the same multigrid routine described here, except we only solve for the three quantities α, β^ρ and β^z during the V-cycle; ψ is then simply considered another 'source function'.)

A key component of the MG solver is the relaxation routine that is designed to *smooth* the residuals associated with the discretized elliptic equations. We use pointwise Newton–Gauss–Seidel relaxation with red-black ordering (see figure 9), simultaneously updating all four quantities (α, β^ρ, β^z, ψ) at each grid point during a relaxation sweep. In addition to its use for the standard pre-coarse-grid-correction (pre-CGC) and post-CGC smoothing sweeps,
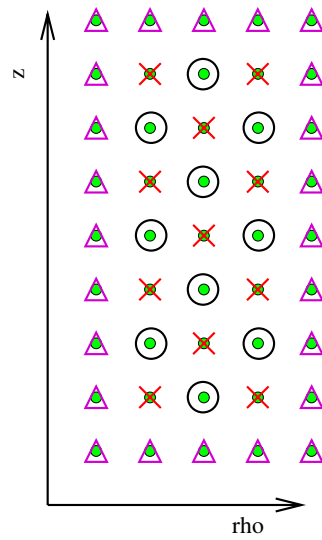
Figure 9. Diagram illustrating the order in which relaxation occurs. Shown here is a 5×9 grid spanning $\rho \times z$ with the grid points represented by filled circles. The Xs denote 'red' (interior) points which are visited first. The Os denote 'black' (interior) points which are visited next. Finally, the triangles denote boundary points which are visited last.

the relaxation routine is also used to *solve* problems on the coarsest grid. We use half-weighted restriction to transfer fields from fine to coarse grids and (bi)linear interpolation for coarse to fine transfers. We generally use three pre-CGC and three post-CGC sweeps per V-cycle, and likewise normally use a single V-cycle per Crank–Nicholson iteration.

One complicating factor here is the treatment of the boundary conditions (39)–(42) and (47)–(50). In accordance with general multi-grid practice, we view the boundary conditions as logically and operationally distinct from the interior equation. The outer boundary conditions can generally be expressed as

$$rX \approx \text{constant}, \tag{A1}$$

where $X \in \{1 - \alpha, 1 - \psi, \beta^z, \beta^\rho\}$. Taking the derivative of (A1) with respect to r, we arrive at the differential form that is applied on the outer boundaries of the computational domain ($\rho = \rho_{\max}, z = z_{\max}, z = -z_{\max}$)

$$X - \rho X_{,\rho} - z X_{,z} = 0. \tag{A2}$$

On the z-axis ($\rho = 0$), conditions (39)–(42) take one of the following two forms

$$A_{i,\rho} = 0 \tag{A3}$$

or

$$A_i = 0. \tag{A4}$$

Equations of the former form are discretized using an $O(h^2)$ backwards difference approximation to the ρ derivative.

The interior and boundary differential equations are solved in tandem via the multigrid approach:

1. The residual is smoothed using some number of relaxation sweeps. For the interior, equations (30)–(32) are relaxed using red-black ordering as discussed above. After each

Table 1. Finite difference operators and their correspondence to differential operators. Here, A_i^n is an arbitrary grid function defined via $A_i^n \equiv A(x_{\min} + (i-1)h, t_{\min} + (n-1)(\lambda h))$, where h and λh are the spatial and temporal grid spacings, respectively. x denotes either of the two spatial coordinates ρ or z, with the dependence of A_i^n on the other suppressed. The parameter ϵ represents a user-specifiable 'amount' of Kreiss–Oliger dissipation.

Operator	Definition	Expansion
$\Delta_x A_i$	$(A_{i+1} - A_{i-1})/(2h)$	$A_{,x}\|_i + O(h^2)$
$\Delta_x^f A_i$	$(-3A_i + 4A_{i+1} - A_{i+2})/(2h)$	$A_{,x}\|_i + O(h^2)$
$\Delta_x^b A_i$	$(3A_i - 4A_{i-1} + A_{i-2})/(2h)$	$A_{,x}\|_i + O(h^2)$
$\Delta_{xx} A_i$	$(A_{i+1} - 2A_i + A_{i-1})/(h^2)$	$A_{,xx}\|_i + O(h^2)$
$\Delta_{xxxx} A_i$	$\Delta_{xx}(\Delta_{xx} A_i) = (A_{i+2} - 4A_{i+1} + 6A_i - 4A_{i-1} + A_{i-2})/h^4$	$A_{,xxxx}\|_i + O(h^2)$
$\Delta_{x^2} A_i$	$(A_{i+1} - A_{i-1})/\left(x_{i+1}^2 - x_{i-1}^2\right)$	$A_{,xx}\|_i + O(h^2)$
$\Delta_x(A_i/x)$	$2(x_{i-1}A_{i+1} - x_{i+1}A_{i-1})/\left(x_{i+1}^2 - x_{i-1}^2\right)/x_i$	$(A/x)_{,x}\|_i + O(h^2)$
$\Delta_x[(\Delta_x A_i)/x]$	$16[x_{i-1/2}A_{i+1} - 2x_i A_i + x_{i+1/2}A_{i-1}]/\left(x_{i+1}^2 - x_{i-1}^2\right)^2$	$(A_{,x}/x)_{,x}\|_i + O(h^2)$
$\mu_t A^n$	$(A^{n+1} + A^n)/2$	$A\|^{n+1/2} + O(\lambda^2 h^2)$
$\Delta_t A^n$	$(A^{n+1} - A^n)/(\lambda h)$	$A_{,t}\|^{n+1/2} + O(\lambda^2 h^2)$
$\Delta_t^\epsilon A^n$	$\Delta_t A^n + \epsilon h^3/(16\lambda)\Delta_{xxxx} A_i^n$	$A_{,t}\|^{n+1/2} + O(\lambda^2 h^2)$

call of this relaxation routine, a second routine that 'relaxes' the boundary points is called[10].

2. For quantities restricted from a fine to a coarse grid, discrete forms of (A3) and (A4) are applied during the V-cycle. At the other boundaries, straightforward injection is used.

The key idea here is to ensure that the boundary relaxation process does not substantially impact the smoothness of the interior residuals, because it is only for smooth residuals that a coarsened version of a fine-grid problem can sensibly be posed.

Finally, in table 1, we show all of the difference operators we use to convert the differential equations listed in III to finite difference form, using the Crank–Nicholson scheme described in section 5. We use Kreiss–Oliger dissipation [30] to maintain smoothness in the evolved fields. Specifically, this involves replacing the Crank–Nicholson time difference operator Δ_t in hyperbolic evolution equations of the form

$$\Delta_t A^n = \mu_t f^n(\ldots) \tag{A5}$$

with the operator Δ_t^ϵ

$$\Delta_t^\epsilon A^n = \mu_t f^n(\ldots). \tag{A6}$$

Empirically, we find that a value of $\epsilon = 0.5$ generally keeps our fields acceptably smooth. For the discretization of spatial derivatives, at all interior grid locations we use the 'centred' difference operators $(\Delta_x, \Delta_{xx}, \ldots)$, while at grid boundaries we use forwards $\left(\Delta_x^f\right)$ or backwards $\left(\Delta_x^b\right)$ operators where appropriate, so as not to reference points outside the computational domain. Furthermore, for $\bar{\sigma}$ and $\bar{\Omega}$, in addition to enforcing the on-axis regularity conditions $\bar{\sigma}(\rho = 0, z, t) = 0$ and $\bar{\Omega}(\rho = 0, z, t) = 0$, we set $\bar{\sigma}(\rho = h, z, t)$ and $\bar{\Omega}(\rho = h, z, t)$ by linear interpolation; i.e. $\bar{\sigma}(\rho = h, z, t) = \bar{\sigma}(\rho = 2h, z, t)/2$ and $\bar{\Omega}(\rho = h, z, t) = \bar{\Omega}(\rho = 2h, z, t)/2$.

[10] A subtle point here concerns the 'relaxation' occurring on the boundaries. The finite difference equations on the boundary yield algebraic equations which determine the given fields there 'exactly'. The subtlety arises because these algebraic conditions couple neighbouring boundary points and thus, despite the fact that we solve these equations exactly, the residual (as computed after the entire boundary is 'relaxed') will not be identically zero. We find this procedure suffices to keep residuals sufficiently smooth over both interior and boundary domains.

Appendix B. The spherically symmetric model

One simple test of the code compares the results for spherically symmetric initial data with the output of a code which explicitly assumes spherical symmetry. Here we present the equations for this 1D code. The spacetime metric is

$$ds^2 = -(\alpha^2 - \psi^4 \beta^2)\,dt^2 + 2\psi^4 \beta\,dt\,dr + \psi^4(dr^2 + r^2\,d\Omega^2), \tag{B1}$$

where α, β and ψ are functions of r and t, $d\Omega^2$ is the line element on the unit 2-sphere, and β is the radial component of the shift vector (i.e. $\beta^i = (\beta, 0, 0)$). Adopting maximal slicing to facilitate direct comparison with the axisymmetric code, we have

$$K^i{}_j = \mathrm{diag}\big(K^r{}_r(r, t), 0, 0\big). \tag{B2}$$

Then a sufficient set of equations for the coupled Einstein-massless-scalar system is [34]

$$\psi'' + \frac{2\psi'}{r} + 2\pi[\Phi^2 + \Pi^2]\psi + \frac{3}{16}\big(K^r_r\big)^2 \psi^5 = 0 \tag{B3}$$

$$\big(K^r{}_r\big)' + 3\frac{(r\psi^2)'}{r\psi^2} K^r{}_r + \frac{16\pi}{\psi^2}\Phi\Pi = 0 \tag{B4}$$

$$\frac{[(r\psi)^2 \alpha']'}{(r\psi)^2} - \left[16\pi \Pi^2 + \frac{3}{2}\psi^4\big(K^r_r\big)^2\right]\alpha = 0 \tag{B5}$$

$$\left(\frac{\beta}{r}\right)' = \frac{3\alpha K^r_r}{2r} \tag{B6}$$

$$\dot{\Phi} = \beta\Phi + \frac{\alpha}{\psi^2}\Pi \tag{B7}$$

$$\dot{\Phi} = \left(\beta\Phi + \frac{\alpha}{\psi^2}\Pi\right)' \tag{B8}$$

$$\dot{\Pi} = \frac{1}{r^2\psi^4}\left[r^2\psi^4\left(\beta\Pi + \frac{\alpha}{\psi^2}\Phi\right)\right]' - \left[\alpha K^r_r + 2\beta\frac{(r\psi^2)'}{r\psi^2}\right]\Pi. \tag{B9}$$

Here dot and prime denote derivatives with respect to t and r, respectively.

The evolution equations (B7)–(B9) are discretized using an $O(h^2)$ Crank–Nicholson scheme. Equations (B3) and (B4) are similarly discretized using $O(h^2)$ finite difference approximations, then solved iteratively for ψ and $K^r{}_r$ at each timestep. Once Φ, Π, ψ and $K^r{}_r$ have been determined, α and β are found from $O(h^2)$ finite difference versions of equations (B5) and (B6). The code is stable and second-order convergent.

References

[1] Smarr L L 1975 *PhD Dissertation* University of Texas at Austin
[2] Eppley K R 1977 *PhD Dissertation* Princeton University
[3] Shapiro S L and Teukolsky S A 1992 Collisions of relativistic clusters and the formation of black holes *Phys. Rev.* D **45** 2739
[4] Anninos P, Hobill D, Seidel E, Smarr L and Suen W 1993 The collision of two black holes *Phys. Rev. Lett.* **71** 2851 (*Preprint* gr-qc/9309016)
[5] Baker J, Abrahams A, Anninos P, Brandt S, Price R, Pullin J and Seidel E 1997 The collision of boosted black holes *Phys. Rev.* D **55** 829
[6] Anninos P and Brandt S 1998 Head-on collision of two unequal mass black holes *Phys. Rev. Lett.* **81** 508 (*Preprint* gr-qc/9806031)

[7] Nakamura T 1981 General relativistic collapse of axially symmetric stars leading to the formation of rotating black holes *Prog. Theor. Phys.* **65** 1876–90

[8] Stark R F and Piran T 1985 Gravitational wave emission from rotating gravitational collapse *Phys. Rev. Lett.* **55** 891

[9] Nakamura T, Oohara K and Kojima Y 1987 General relativistic collapse of axially symmetric stars *Prog. Theor. Phys. Suppl.* **90** 13

[10] Shibata M 2000 Axisymmetric simulations of rotating stellar collapse in full general relativity—criteria for prompt collapse to black holes *Prog. Theor. Phys.* **104** 325

[11] Shibata M 2003 Axisymmetric general relativistic hydrodynamics: long-term evolution of neutron stars and stellar collapse to neutron stars and black holes *Preprint* gr-qc/0301103

[12] Abrahams A M, Cook G B, Shapiro S L and Teukolsky S A 1994 Solving Einstein's equations for rotating space-times: evolution of relativistic star clusters *Phys. Rev.* D **49** 5153

[13] Shapiro S L and Teukolsky S A 1991 Formation of naked singularities: the violation of cosmic censorship *Phys. Rev. Lett.* **66** 994

[14] Garfinkle D and Duncan G C 2001 Numerical evolution of Brill waves *Phys. Rev.* D **63** 044011 (*Preprint* gr-qc/0006073)

[15] Alcubierre M, Brandt S, Brugmann B, Holz D, Seidel E, Takahashi R and Thornburg J 2001 Symmetry without symmetry: numerical simulation of axisymmetric systems using Cartesian grids *Int. J. Mod. Phys.* D **10** 273

[16] Brandt S, Font J A, Ibanez J M, Masso J and Seidel E 2000 Numerical evolution of matter in dynamical axisymmetric black hole spacetimes *Comput. Phys. Commun.* **124** 169

[17] Brandt S and Seidel E 1995 The evolution of distorted rotating black holes: I. Methods and tests *Phys. Rev.* D **52** 856

[18] Brandt S and Seidel E 1995 The evolution of distorted rotating black holes: II. Dynamics and analysis *Phys. Rev.* D **52** 870

[19] Brandt S and Seidel E 1996 The evolution of distorted rotating black holes: III. Initial data *Phys. Rev.* D **54** 1403

[20] Abrahams A M and Evans C R 1992 Trapping a geon: black hole formation by an imploding gravitational wave *Phys. Rev.* D **46** 4117

[21] Abrahams A M and Evans C R 1993 Critical behaviour and scaling in vacuum axisymmetric gravitational collapse *Phys. Rev. Lett.* **70** 2980

[22] Maeda K, Sasaki M, Nakamura T and Miyama S 1980 A new formalism of the Einstein equations for relativistic rotating systems *Prog. Theor. Phys.* **63** 719

[23] Maeda K 1983 [(2+1)+1]-dimensional representation of the Einstein equations *Proc. 3rd Marcel Grossmann Meeting on General Relativity* ed Hu Ning (London: Science Press)

[24] Geroch R 1971 A method for generating solutions of Einstein's equations *J. Math. Phys.* **12** 918

[25] Misner C W, Thorne K S and Wheeler J A 1973 *Gravitation* (New York: Freeman)

[26] Bardeen J M and Piran T 1983 General relativistic axisymmetric rotating systems: coordinates and equations *Phys. Rep.* **96** 205

[27] Appelquist T, Chodos A and Freund P G O 1987 *Modern Kaluza-Klein Theories* (Reading, MA: Addison-Wesley)

[28] Thornburg J 1996 Finding apparent horizons in numerical relativity *Phys. Rev.* D **54** 4899

[29] Alcubierre M, Brandt S, Brugmann B, Gundlach C, Masso J, Seidel E and Walker P 2000 Test beds and applications for apparent horizon finders in numerical relativity *Class. Quantum Grav.* **17** 2159

[30] Kreiss H-O and Oliger J 1973 *Methods for the Approximate Solution of Time Dependent Problems* Global Atmospheric Research Program Publication No 10 (World Meteorological Organization, Case Postale No. 1, CH-1211 Geneva 20, Switzerland)

[31] Software available from http://laplace.physics.ubc.ca/Members/matt/Rnpl/index.html

[32] Brandt A 1977 MultiLevel adaptive solutions to boundary value problems *Math. Comput.* **31** 333–90

[33] Brandt A 1982 Guide to multigrid development *Lecture Notes in Mathematics* vol 960 (New York: Springer-Verlag) pp 220–312

[34] Choptuik M W 1982 A study of numerical techniques for radiative problems in general relativity *PhD Thesis* The University of British Columbia